Soft X-Ray Emission and Meta-Stable Population Dynamics in Sm-Like Pb and Neighboring Ions

Dingbao SONG[1)]*, Hayato OHASHI[2)], Hiroyuki A. SAKAUE[3)],
Nobuyuki NAKAMURA[4)], Naoki KIMURA[3)], Daiji KATO[1,3)]

[1)] *Interdisciplinary Graduate School of Engineering Sciences, Kyushu University, Kasuga, Fukuoka 816-8580, Japan*
[2)] *Institute of Liberal Arts and Sciences, University of Toyama, Toyama, Toyama 930-8555, Japan*
[3)] *National Institute for Fusion Science, National Institutes of Natural Sciences, Toki, Gifu 509-5292, Japan*
[4)] *Institute for Laser Science, The University of Electro-Communications, Chofu, Tokyo 182-8585, Japan*

In recent years, the development of soft X-ray (SXR) light sources has progressed rapidly, particularly for applications within the water window region (23–44 Å), where high-resolution, high-contrast imaging of biological cells and macromolecules is possible. In this study, we analyze water window emission lines of samarium-like (Sm-like) Pb^{20+} ions observed using a compact electron beam ion trap at an electron beam energy of 565 eV. The analysis is carried out using a collisional-radiative model based on atomic data from HULLAC. Three distinct meta-stable states of Pb^{20+}, each with a fractional population exceeding 1%, are identified. To explore the conditions under which meta-stable states are formed or suppressed across the isoelectronic sequence, we performed systematic atomic structure and transition rate calculations for Sm-like ions from Hg to Po ($Z = 80$–84). These results provide new insights into the role of energy level crossings and decay pathways in the formation of long-lived states, offering implications for optimizing soft X-ray emission in plasma-based light sources.

1. Introduction

Soft X-ray radiation has emerged as a major research focus in recent years because of its broad applications in biology, materials science, and plasma diagnostics [1–3]. Within this landscape, heavy-element highly charged ions (HCIs) are particularly noteworthy: their complex electronic structures produce strong soft X-ray line emission [4, 5]. Many of emission lines fall within the water window (23–44 Å) where water is transparent but carbon-based materials absorb strongly, enabling high-contrast imaging and precise diagnostics [6].

To interpret these complex spectra in a systematic way, studies along isoelectronic sequences are especially effective [7–9]. By comparing ions with the same number of electrons but different elements, one can trace trends in energy levels, transition rates, and the persistence of metastable states, while clarifying the roles of relativistic effects and electron correlation. Such comparisons reveal how atomic structure evolves across a sequence and provide predictive insight into spectral behavior under varying plasma conditions. Although experimentally demanding, systematic isoelectronic studies offer essential benchmarks for theory and deepen our understanding of atomic processes in HCIs. Within this context,

samarium-like (Sm-like) ions (62 electrons) have attracted particular attention due to their rich soft X-ray spectra and the emergence of long-lived meta-stable excited states [9–12]. For instance, in the case of Bi^{21+}, two such meta-stable states: $[4f_{7/2}^{-1}5p_{1/2}]_4$ [13] and $[4f^{14}5s5p_{1/2}]_0$ [9, 10], have been shown to reach fractional populations exceeding 1%, significantly influencing emission features within the water window [13].

To evaluate whether similar or new meta-stable states appear in neighboring elements, we first performed experiments on Sm-like lead (Pb^{20+}), using the compact electron beam ion trap (CoBIT) [14], at the National Institute for Fusion Science, designated as CoBIT-II [15]. In parallel, we carried out collisional–radiative simulations for the entire Sm-like isoelectronic sequence from Hg to Po ($Z = 80$–84). For elements where experiments are particularly challenging, the analysis relies primarily on theoretical modeling. Using a collisional–radiative model (CRM) at an electron density of 10^{10} cm^{-3}, we analyze the population kinetics and soft X-ray spectral signatures of Pb^{20+} to quantify the influence of meta-stable states. Based on the theoretical analyses, the present work identifies a new meta-stable state, $[4f_{7/2}^{-1}5p_{1/2}]_3$, which has a large fractional population in Pb^{20+} ions, and theoretically predicts the energy level evolution and spectral features of other ions. These results provide valuable benchmarks for the atomic structure and radiative behavior of heavy-element

Corresponding author's e-mail: song.dingbao.042@s.kyushu-u.ac.jp

HCIs relevant to soft X-ray plasma diagnostics.

In Sec. 2, we explain the experimental measurements of the Sm-like Pb^{20+} spectra with CoBIT-II. In addition, a method for modeling the baseline is also introduced. In Sec 3. in order to simulate the behavior of Pb^{20+} ions in CoBIT-II, we construct a CRM. Complete sets of atomic data are provided by *ab initio* HULLAC calculations [16], and the CRM simulations are carried out using an external implementation based on our own code. In Sec. 4, we compare calculated and experimental spectra from CoBIT-II for Sm-like Pb and Bi and evaluated CRM predictions for Sm-like mercury (Hg, $Z = 80$) to polonium (Po, $Z = 84$), analyzing the spectral features in each case. Finally, we conclude with a summary of the key findings.

2. Experiment

The CoBIT-II device comprises an electron gun, a superconducting coil, drift-tube electrodes, and an electron collector. The electron gun generates an electron beam that is compressed radially by the magnetic field of the superconducting coil and guided through the drift-tube assembly to the collector. Ions are confined axially by potentials applied to the drift tubes and radially by the space-charge potential of the compressed beam. Within this environment, successive electron impact ionization produces HCIs, with the electron beam typically reaching a density of $\sim 10^{10}$ cm^{-3} under ultra-high vacuum conditions of 10^{-8} Pa.

The experimental conditions were the same as those for Sm-like Bi [13], except for the electron-beam energy, which was 600 eV for Bi and 565 eV for Pb. Pb vapor also was infused into CoBIT-II using a K-cell [17], and soft X-ray spectra were measured using a spectrometer with a 2,400 grooves mm^{-1} grating (30-001, Shimadzu Corporation) [18] and a back-illuminated EUV-sensitive CCD (PIXIS-XO400B). A 0.15 μm thick aluminum filter was employed to suppress visible stray light from a cathode of the electron gun. Wavelength calibration was performed using Fe XVII lines in the 15–35 Å range, which has a standard deviation of 0.02 Å relative to the NIST ASD [19]. Intensity corrections considered the wavelength dependence of CCD quantum efficiency (decreasing from 0.73 to 0.51 between 20 and 36 Å), aluminum filter transmission, and grating reflectivity (falling from 0.03 to 0.02), all of which monotonically decline with wavelength.

In CoBIT experiments, the spectral baseline primarily arises from strong stray light from the cathode of the electron gun, producing a continuum background that must be considered to isolate the true line emissions. In this study, the Chauvenet criterion [20] was first employed to exclude peak-related data points, then the Asymmetric Least Squares (ALS) algorithm [21] was applied to the remaining (peak-removed) data for baseline fitting.

The ALS parameters were further optimized using Bayesian optimization [22], with the no peak range 10–20 Å, which is not presented in this paper, serving as a prior constraint. According to the Chauvenet criterion, a data point y_i is excluded when its normalized deviation exceeds a critical threshold:

$$z_i = \frac{|y_i - \mu|}{\sigma}, \qquad z_i \geq z_{crit}, \tag{1}$$

where μ and σ denote the mean and standard deviation, respectively. The ALS baseline was then determined by minimizing the penalized least-squares functional:

$$J(z) = \sum_{i=1}^{N} w_i(y_i - z_i)^2 + \lambda \sum_{i=1}^{N} (\Delta^2 z_i)^2, \tag{2}$$

where λ is the smoothing parameter, w_i are adaptive weights, and $\Delta^2 z_i$ represents the second-order difference operator. This procedure yields an optimized baseline experimental spectrum for Sm-like Pb^{20+}. The same approach is adopted also for the experiment spectrum of Sm-like Bi^{21+}.

3. Simulation Method

Given the low-density and non-local thermodynamic equilibrium (non-LTE) nature of CoBIT plasmas, the level populations are determined by complex atomic processes. Different with the laser-produced plasma experiments, which are inherently transient and time-dependent, the CoBIT provides a quasi–steady-state plasma environment. Within the trap, ions confined by electrostatic potentials continuously interact with a mono-energetic electron beam with a constant density. As a result, the CoBIT plasma can be treated as time-independent, enabling the application of a steady-state CRM to describe its exited state population kinetics and emission characteristics. The population of each excited level i at steady state is governed by the rate equation:

$$n_e \sum_{j \neq i} C_{ji} n_j + \sum_{j > i} A_{ji} n_j$$
$$= \left(n_e \sum_{j \neq i} C_{ij} + \sum_{i > j} A_{ij} + n_e S_i \right) n_i, \tag{3}$$

where the terms on the left-hand side represent the in-flow of population into level i, arising from electron-impact (de-)excitation from other levels ($n_e C_{ij} n_j$) and radiative cascades from higher-lying levels ($A_{ij} n_j$ for $j > i$). The right-hand side, in contrast, describes the out-flow of population from level i, including collisional (de-)excitation to other levels ($n_e C_{ji} n_i$), spontaneous radiative decay to lower levels ($A_{ji} n_i$ for $j < i$) and the electron impact ionization to higher charge state from level i ($n_e S_i$).

In the present CRM calculations, radiative recombination was neglected due to the relatively high electron beam energies, 565 eV, where its contribution is minimal. Dielectronic recombination (DR), while potentially significant at specific resonance energies associated with autoionizing levels, was also omitted for simplicity, as it primarily affects narrow energy ranges and does not substantially influence excited level population under the present conditions.

The radiative transitions considered in the calculations comprise electric dipole (E1), electric quadrupole (E2), electric octupole (E3), magnetic dipole (M1), and magnetic

Table 1. Electronic configurations ($n = 5$–6, $m = 5$–7, $k = 5$–8 and $l \leq 4$) for Pb^{19+}–Pb^{21+} ions and the level number included in the present CRM for each ion.

Pb^{19+}	$\boldsymbol{4f^{14}5s^2 5p}$ $4f^{14}(5s^2\,kl,\,5s\,5p^2,\,5s\,5p\,kl,\,5p^3)$ $4f^{13}(5s^2\,5p^2,\,5s^2\,5p\,kl)$ $4f^{13}(5s\,5p^3,\,5s\,5p^2\,ml,\,5p^4)$ $4f^{12}\,5s^2\,5p^2\,nl$ $4d^9\,4f^{14}\,5s^2(5p^2,\,5p\,5l)$	13000 (22704)
Pb^{20+}	$\boldsymbol{4f^{14}5s^2}$ $4f^{14}(5s\,kl,\,5p^2)$ $4f^{13}(5s^2\,kl,\,5s\,5p^2,\,5s\,5p\,kl)$ $4f^{12}\,5s^2(5p^2,\,5p\,ml)$ $4d^9\,4f^{14}\,5s^2\,5l$ $4d^9\,4f^{13}\,5s^2\,5p\,5l$	6769 (16677)
Pb^{21+}	$\boldsymbol{4f^{14}5s}$, $\boldsymbol{4f^{14}kl}$ $4f^{13}(5s^2,\,5s\,ml,\,5p^2,\,5p\,5l)$ $4f^{12}\,5s^2\,kl$ $4d^9(4f^{14}\,5s^2,\,4f^{14}\,5s\,5l,\,4f^{13}\,5s^2\,5l)$	3064 (3873)

The number in the parenthesis is the total number of levels for each ion. The bolded configuration denotes the ground states of each charge state.
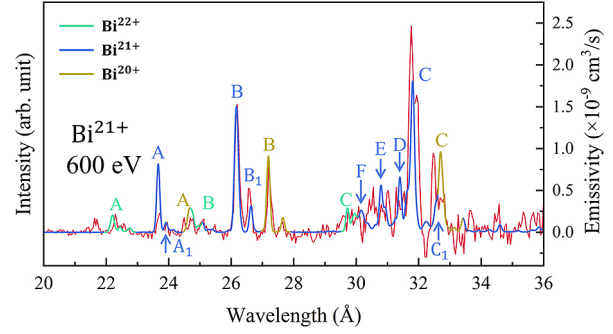

Fig. 1. Emission line spectra of highly charged Sm-like Bi ions in CoBIT (red) and calculated EUV spectra in the water window range. The wavelength scales of the calculated spectra for Bi^{20+}, Bi^{21+} and Bi^{22+} are shifted +0.14, +0.15, and +0.31 Å, respectively. The calculated spectra have been convoluted with Gaussian distribution functions with a full-width at half-maximum of 0.12 Å.

quadrupole (M2) transitions, with all rates obtained using fully relativistic wave functions based on optimized parametric potentials. To account for electron correlation effects, the relativistic configuration interaction (RCI) calculations included single and double electron excitation configurations. These were systematically constructed to cover three types of correlations: core-core (CC), core-valence (CV), and valence-valence (VV), where electrons are promoted from and to core or valence orbitals accordingly. Electron-impact excitation and ionization cross sections were computed using the fully relativistic distorted-wave (DW) approximation. Table 1 provides an overview of the electronic configurations employed for Pb^{19+} to Pb^{21+} ions in this study, together with the total number of energy levels incorporated into the CRM calculations.

4. Results and Discussion

4.1 Emission line spectra of Sm-like Pb^{20+} ions with contributions from adjacent charge states

In our previous study [13], we investigated the soft X-ray emission of Sm-like Bi^{21+}, and clarified its meta-stable states and transitions in the water window range. Figure 1 presents a comparison between the experimental spectrum of Sm-like Bi^{21+} at 600 eV and simulated spectra composed of multiple charge states. Strong peaks A, B, and C are due to the $4f$–$7g, 6g, 5g$ transitions, respectively. The transitions of the other peaks are indicated in Table 2. The spectrum of each charge state is weighted by its respective abundance also evaluated in our previous work [13], i.e. 67.5% for Bi^{21+}, while 27.1% for Bi^{20+} and 8% for Bi^{22+}.

In the figure, the yellow line represents simulated emission lines from europium-like (Eu-like) Bi^{20+}. The blue line corresponds to Sm-like Bi^{21+}, which dominates the spectrum, while the green line originates from promethium-like (Pm-like) Bi^{22+}.

Although the electron beam energy (600 eV) is below the first ionization threshold of Bi^{21+} (611 eV [13]), Bi^{22+} can be created via ionization from the meta-stable excited levels of Bi^{21+}: $[4f_{7/2}^{-1}5p_{1/2}]_4$ and $[4f^{14}5s5p_{1/2}]_0$.

At 565 eV, a similar study is conducted for Sm-like Pb^{20+}, and Fig. 2 also presents a comparison between the experimental and abundance-weighted simulated spectra. The ion abundance was evaluated as follows. The peak B was selected for each charge state to evaluate the ion abundance, as other peaks were not suitable due to overlap or lack of isolation. Each peak area was approximated using a Gaussian distribution function. Assuming that the area of a given peak, $A^{(z)}$, is proportional to the ion abundance N_z multiplied by the total line emissivity $\varepsilon^{(z)} = \sum_\lambda \varepsilon_\lambda^{(z)}$—as calculated by the present CRM at the relevant electron beam energy—the abundance ratio between adjacent charge states is given by:

$$\frac{A^{(z)}}{A^{(z-1)}} = \frac{\varepsilon^{(z)}}{\varepsilon^{(z-1)}} \cdot \frac{N_z}{N_{z-1}}. \qquad (4)$$

Evaluated fractional ion abundance as: Pb^{20+} represents 68.3 ($\pm$0.25)%, while Pb^{19+} makes up 21.7($\pm$1.58)% and Pb^{21+} accounts for 10%. The uncertainty in each ion abundance is evaluated from the uncertainty in the peak area obtained through Gaussian fitting, except for the fractional abundance of Pb^{21+} at 565 eV, which is adjusted based on the peak height in the 26–27 Å wavelength range. The presence of Pm-like Pb^{21+} can be explained similarly as for Bi^{22+}. Despite the electron energy is below the ionization potential, ionization from meta-stable excited levels enable the formation of higher charge states. Such ionization mediated via meta-stable excited levels has been reported in a number of previous works as well [23–29].

Figure 2 shows that the calculated spectra agree well with the experimental results, by systematically shifting the theoretical wavelengths to longer values by +0.19, +0.17, and +0.16 Å, for Pb^{19+}, Pb^{20+} and Pb^{21+}, respectively. By comparing Figs. 1 and 2, it is evident that, similar to the Bi spectrum at 600 eV, the Pb spectrum at 565 eV also exhibits strong peaks A, B, and C, which correspond to Eu-, Sm-, and

Table 2. Emission lines of Eu-like to Pm-like ions.

Ions	Label	Bi		Pb		Upper state			Lower state
		λ_{ex} [13]	λ_{cal} [13]	λ_{ex}	λ_{cal}	config.	J_{Bi}	J_{Pb}	
Eu-like	A	24.69	24.61	26.86	26.68	$4f_{5/2}^{-1}5p_{1/2}7g_{7/2}$	$\frac{1}{2},\frac{3}{2}$	$\frac{3}{2},\frac{3}{2}$	
	B	27.17	27.03	29.47	29.28	$4f_{5/2}^{-1}5p_{1/2}6g_{7/2}$	$\frac{3}{2},1$	$\frac{3}{2},1$	$[4f^{14}5p_{1/2}]_{\frac{1}{2}}$
	C	32.75	32.55	35.37	35.11	$4f_{5/2}^{-1}5p_{1/2}5g_{7/2}$	$\frac{3}{2},\frac{1}{2},\frac{3}{2}$	$\frac{3}{2},\frac{3}{2},\frac{1}{2}$	
Sm-like	A	23.70	23.52	25.60	25.45	$4f_{5/2}^{-1}7g_{7/2}$	1	1	
	A_1	23.92	23.77	25.80	25.66	$4f_{7/2}^{-1}7g_{9/2}$	1,1	1,1	
	B	26.17	26.02	28.31	28.14	$4f_{5/2}^{-1}6g_{7/2}$	1,1	1,1	
	B_1	26.58	26.49	28.72	28.62	$4f_{7/2}^{-1}6g_{9/2}$	1	1	
	C	31.75	31.66	—	34.1	$4f_{5/2}^{-1}5g_{7/2}$	1	1	$[4f^{14}5s^2]_0$
	C_1	32.47	32.41	34.98	34.9	$4f_{7/2}^{-1}5g_{9/2}$	1	1	
	D	—	30.65	33.68	33.61	$4f_{7/2}^{-1}5g_{9/2}$	1	1	
	E	—	31.26	—	32.43	$4d_{3/2}^{-1}5p_{1/2}$	1	1	
	F	—	30.03	—	31.95	$4d_{5/2}^{-1}5p_{3/2}$	1	1	
Pm-like	A	—	21.94	—	23.73	$4f_{5/2}^{-1}4f_{7/2}^{-1}7g_{7/2}$	$\frac{5}{2},\frac{3}{2},\frac{3}{2},\frac{3}{2}$	$\frac{5}{2},\frac{9}{2},\frac{7}{2}$	
	B	—	24.36	—	26.27	$4f_{5/2}^{-1}4f_{7/2}^{-1}6g_{7/2}$	$\frac{5}{2},\frac{9}{2},\frac{9}{2},\frac{7}{2}$	$\frac{5}{2},\frac{7}{2}$	$[4f_{7/2}^{-1}5s^2]_{\frac{7}{2}}$
	C	—	29.44	—	31.84	$4f_{5/2}^{-1}4f_{7/2}^{-1}5g_{7/2}$	$\frac{9}{2}$	$\frac{5}{2},\frac{9}{2},\frac{7}{2}$	

λ_{ex} represents the peak centers extracted from Gaussian fits to the experimental spectra, while λ_{cal} denotes the central wavelengths obtained from Gaussian fitting of the simulated spectra. J includes the total angular momentum of the strongest emission line, along with those of other lines whose emissivities exceed half of the strongest line, listed in descending order of emissivity. The unit of wavelength is Å. The overall uncertainty of the experimental wavelengths is estimated to be ±0.02 Å. The unit of wavelength is Å.
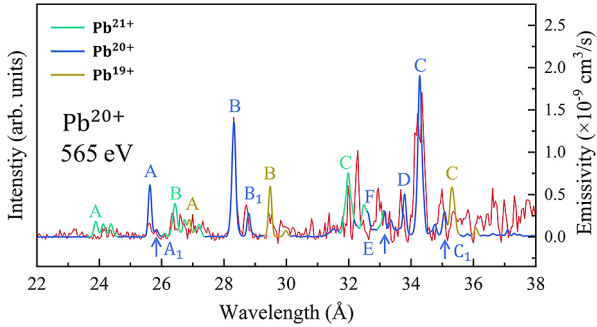

Fig. 2. Emission line spectra of highly charged Sm-like Pb ions in CoBIT (red) and calculated EUV spectra in the water window range. The wavelength scales of the calculated spectra for Pb^{19+}, Pb^{20+} and Pb^{21+} are shifted +0.19, +0.17, and +0.16 Å, respectively. The calculated spectra have been convoluted with Gaussian distribution functions with a full-width at half-maximum of 0.12 Å.

Pm-like $4f-7, 6, 5g$ transitions, respectively, as shown in Table 2. In addition, in Sm-like Pb, weaker peaks A_1, B_1, and C_1 are observed, arising from different relativistic orbitals. Peak D can be designated to the $4f-5g$ transition. However, when the effects of RCI are considered, the $5s-7p$ configuration contributes comparably to the wavefunction. Both of the peaks E and F correspond to $4d-5p$ transitions, but different relativistic orbitals.

Table 2 compares the central wavelengths of each peak in the experimental spectra with those calculated using the present CRM, based on atomic data from HULLAC. Experimental wavelengths were obtained by fitting each peak with a single Gaussian function, while CRM wavelengths were determined by averaging the peak positions of the corresponding transition arrays. The uncertainty in the experimental wavelengths arises mainly from wavelength calibration, which dominates over the fitting error. Accordingly, the overall uncertainty is estimated to be ± 0.02 Å. Theoretical wavelengths for peaks A, B, and C show reasonable agreement with the experimental values, all within 0.2 Å.

Table 2 also compares the transitions from Eu-like to Pm-like ions for both Pb and Bi. It is evident that, for the same transition, the calculated and experimental wavelengths of Pb are systematically longer than those of Bi, regardless of the isoelectronic sequence. In the present theoretical study, a distinct difference was found in the population of the level $[4f_{7/2}^{-1}5p_{1/2}]_3$ between Sm-like Pb^{20+} and Bi^{21+}, indicating that this level becomes meta-stable only in Pb^{20+}, even though the same configuration set was employed. Such differences highlight the importance of systematic studies across the isoelectronic sequence. Therefore, in addition to Sm-like Bi and Pb, we have also investigated the neighboring elements to examine how their atomic structures and meta-stable populations evolve.

4.2 Calculated spectra of Sm-like highly charged high Z ions

To extend our investigation beyond Pb and Bi, we analyzed neighboring Sm-like ions, including mercury (Hg, Z = 80), thallium (Tl, Z = 81) and polonium (Po, Z = 84), at electron-beam energies 480, 520, and 650 eV, which are below calculated ionization thresholds (488, 528, and 654 eV), respectively, in order to judge whether the presence of additional meta-stable states is peculiar to Pb[20+] or a common feature among adjacent elements in the Sm-like isoelectronic sequence.

Figure 3 shows the calculated spectra of Sm-like highly charged Hg to Po ions in the water window wavelength range. As the atomic number increases, the peaks of the transitions consistently shift toward shorter wavelengths, as observed in both the experimental and calculated comparisons between Bi and Pb. The spectra reveal several transition arrays: $4f$–$7g$ (peak A), $4f$–$6g$ (peak B), $4f$–$5g$ (peak C, D, I and J), $4d$–$5p$ (peak E and F), $4d$–$4f$ (peak G and H). Table 3 lists the calculated central wavelengths derived from the transition arrays of the identified configurations. The peaks G and H are due to the $4d$–$4f$ inner-shell transitions. The peaks I and J have the common lower level: $[4f_{7/2}^{-1}5p_{1/2}]_4$, while the peak J contains another line from $[4f_{7/2}^{-1}5p_{1/2}]_3$. Both of them are strongly meta-stable.

Table 4 shows detailed population rates and populations for the long-lived meta-stable states $[4f_{7/2}^{-1}5p_{1/2}]_3$, $[4f_{7/2}^{-1}5p_{1/2}]_4$ and $[4f^{14}5s5p_{1/2}]_0$ in Sm-like highly charged ions from Hg to Po in CoBIT. As shown in the table, the dominant rates influencing the populations of meta-stable states $[4f_{7/2}^{-1}5p_{1/2}]_4$ and $[4f^{14}5s5p_{1/2}]_0$ are those of in-flow via radiative cascades (In-rad) from higher levels: $\sum_{j>i} A_{ij} n_j$ and out-flow by collisional (de)excitation (Out-col): $n_e \sum_{j \neq i} C_{ji}$. For the state $[4f_{7/2}^{-1}5p_{1/2}]_4$, both In-rad and Out-col rates increase as the atomic number decreases. However, since the In-rad rate grows more rapidly than the Out-col rate, the overall population of $[4f_{7/2}^{-1}5p_{1/2}]_4$ increases. In the case of $[4f^{14}5s5p_{1/2}]_0$, the In-rad rate increases from $Z = 84$ to $Z = 82$, but then declines from $Z = 82$ to $Z = 80$, while the Out-col rate continues to rise across the entire range, resulting in a net decrease in population. The state $[4f_{7/2}^{-1}5p_{1/2}]_3$ exhibits a dis-

tinct behavior. Similar to $[4f_{7/2}^{-1}5p_{1/2}]_4$, its In-rad and Out-col rates also increase with decreasing atomic number. However, for Po and Bi, the Out-rad rate is significantly larger than the other rates, strongly affecting the balance and leading to very low populations. In contrast, for Pb, although the Out-rad rate remains relatively high, it does not dominate the population dynamics, giving the population of 1.40%. For Tl and Hg, a substantial drop in the Out-rad rate leads to a marked increase in the population of $[4f_{7/2}^{-1}5p_{1/2}]_3$.

In Fig. 4, symbols indicate fractional populations of the ground state and the meta-stable states. As the atomic number increases, both of the ground state (black square) and the meta-stable state $[4f^{14}5s5p_{1/2}]_0$ (red circle) which is strictly forbidden for radiative decay to the ground state via one-photon emission as it is $J = 0 \rightarrow J = 0$ transition, grow in their fractional populations, while the fractional populations of the other meta-stable states, $[4f_{7/2}^{-1}5p_{1/2}]_3$ (purple circle) and $[4f_{7/2}^{-1}5p_{1/2}]_4$ (yellow star), show a declining trend with the atomic number.

Figure 4 also displays the energy levels below 100 eV for Sm-like ions from Hg to Po.
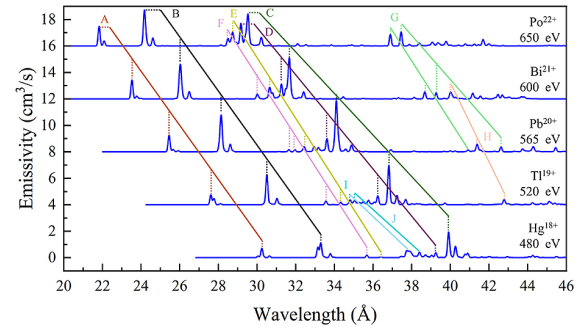

Fig. 3. The EUV spectra for the Sm-like sequence, corresponding to elements with atomic numbers Z = 80–84, were computed using the HULLAC. Peak A, B and C are the $4f$–$7g$, $6g$, $5g$ transition, respectively. Peak D is also the $4f$–$5g$ transition, but due to strong configuration mixing in the upper level, the $5s$–$7p$ transition is mixed. Peak E and F are $4d$–$5p$ transitions. Peak G and H are $4d$–$4f$ transitions. Peak I and J are $4f$–$5g$ transitions from meta-stable states. The details of these transitions are presented in Table 3.

Table 3. Calculated central wavelength obtained from Gaussian fitting. The unit is Å.

Ions	A	B	C	D	E	F	G_L	G_R	H	I	J
Po	21.83	24.14	29.52	29.16	28.74	28.49	36.90	37.45	—	—	—
Bi	23.53	26.03	31.66	31.26	30.65	30.10	38.67	39.26	40.01	—	—
Pb	25.45	28.14	34.10	33.61	32.43	31.95	40.92	42.62	41.38	—	—
Tl	27.61	30.51	36.81	36.24	34.33	33.56	—	—	42.78	34.82	35.04
Hg	30.25	33.30	39.91	39.24	—	35.68	—	—	—	37.74	38.40

A: $[4f_{5/2}^{-1}7g_{7/2}]_1 - [4f^{14}5s^2]_0$

B: $[4f_{5/2}^{-1}6g_{7/2}]_1 - [4f^{14}5s^2]_0$

C: $[4f_{5/2}^{-1}5g_{7/2}]_1 - [4f^{14}5s^2]_0$

D: $[4f_{5/2}^{-1}5g_{7/2}]_1 - [4f^{14}5s^2]_0$ ($[4f^{14}5s7p_{1/2}]_1 - [4f^{14}5s^2]_0$)

E: $[4d_{3/2}^{-1}5p_{1/2}]_1 - [4f^{14}5s^2]_0$

F: $[4d_{5/2}^{-1}5p_{3/2}]_1 - [4f^{14}5s^2]_0$

G: $[4d_{3/2}^{-1}5d_{3/2}]_1 - [4f_{5/2}^{-1}5d_{3/2}]_1$

H: $[4d_{3/2}^{-1}5p_{1/2}]_1 - [4f_{5/2}^{-1}5p_{1/2}]_1$

I: $[4f_{5/2}^{-1}4f_{7/2}^{-1}5p_{1/2}5g_{7/2}]_5 - [4f_{7/2}^{-1}5p_{1/2}]_4$

J: $[4f_{5/2}^{-1}4f_{7/2}^{-1}5p_{1/2}5g_{7/2}]_{5(3)} - [4f_{5/2}^{-1}5p_{1/2}]_{4(3)}$

Table 4. Detailed population rates and populations for the long-lived meta-stable states $[4f_{7/2}^{-1}5p_{1/2}]_3$, $[4f_{7/2}^{-1}5p_{1/2}]_4$, and $[4f^{14}5s5p_{1/2}]_0$ in Sm-like highly charged ions from Hg to Po in CoBIT, where In-col denotes population into state i via collisional (de)excitation ($n_e\sum_{j\neq i}C_{ij}n_j$), In-rad means population through radiative cascades from higher levels ($\sum_{j>i}A_{ij}n_j$), Out-col is depopulation from state i by collisional (de)excitation ($n_e\sum_{j\neq i}C_{ji}$), and Out-rad denotes depopulation via radiative decay to lower states ($\sum_{j<i}A_{ji}$). n_i is the fractional population in %. Parenthetical values represent powers of ten.

| States	Ions	In-col	In-rad	Out-col	Out-rad	n_i (%)
	Po	1.53 (−3)	2.19	190	3.59 (5)	6.11 (−4)
	Bi	2.24 (−3)	2.63	206	6.50 (4)	1.49 (−3)
$[4f_{7/2}^{-1}5p_{1/2}]_3$	Pb	6.43 (−3)	5.67	223	1.84 (2)	1.40
	Tl	3.36 (−2)	28.7	251	1.35 (−4)	11.4
	Hg	5.96 (−2)	53.6	266	6.08 (−6)	20.1
	Po	1.30 (−5)	2.03	185	1.29 (−1)	1.10
	Bi	5.02 (−5)	2.74	201	1.10 (−1)	1.37
$[4f_{7/2}^{-1}5p_{1/2}]_4$	Pb	3.50 (−3)	7.67	217	1.02 (−1)	3.53
	Tl	3.20 (−2)	39.8	247	9.74 (−2)	16.2
	Hg	6.35 (−2)	66.7	261	9.37 (−2)	25.5
	Po	1.23 (−2)	5.82	132	0	4.41
	Bi	1.47 (−2)	6.04	141	0	4.28
$[4f^{14}5s5p_{1/2}]_0$	Pb	1.57 (−2)	6.52	153	0	4.26
	Tl	1.36 (−2)	5.98	168	0	3.58
	Hg	1.17 (−2)	4.79	185	0	2.59
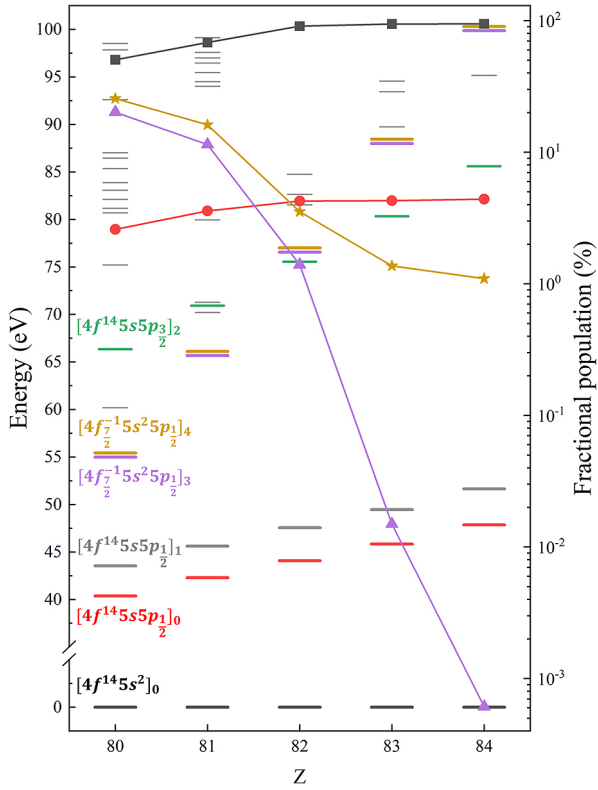
Fig. 4. Calculated energy and fractional population diagram of Sm-like highly charged Hg to Po ions. Horizontal lines represent energy levels, and the color of each configuration corresponds to that of its associated levels. Symbols indicate fractional populations: black squares for ground state $[4f^{14}5s^2]_0$, red circles for meta-stable state $[4f^{14}5s5p_{1/2}]_0$, yellow stars for meta-stable state $[4f_{7/2}^{-1}5p_{1/2}]_4$, and purple triangles for excited state $[4f_{7/2}^{-1}5p_{1/2}]_3$.

For the state $[4f_{7/2}^{-1}5p_{1/2}]_3$ (purple), which exhibits the large Out-rad rate for Po, Bi, and Pb, the primary decay channel is only to the state $[4f^{14}5s5p_{3/2}]_2$ (green). While this transition would appear forbidden as a two-electron one-photon (TEOP) process in a single-configuration picture, the inclusion of RCI provides alternative pathways that render it weakly allowed. For Pb, Bi, and Po, the dominant configuration of the wavefunction accounts for over 99%, while the TEOP-enabling configurations contribute only 0.35%, 0.31%, and 0.27%, respectively. As shown in the figure, the energy difference between these two states increases systematically with atomic number, from 0.45 eV in Pb to 7.65 eV in Bi and 14.27 eV in Po. Because these states decay through only one radiative channel, the decay rate is directly equal to the Einstein spontaneous emission coefficient (A-value), which scales as $A \propto (\Delta E)^3$. So that, the larger transition energies in Bi and Po lead to much higher A-values, making their Out-rad rates substantially larger than that of Pb.

Additionally, a level crossing occurs between Tl and Pb: for Pb, Bi and Po, the energies of $[4f_{7/2}^{-1}5p_{1/2}]_4$ (yellow) and $[4f_{7/2}^{-1}5p_{1/2}]_3$ (purple) are higher than that of $[4f^{14}5s5p_{3/2}]_2$ (green), whereas for Hg and Tl, $[4f^{14}5s5p_{3/2}]_2$ (green) has higher energy. As a consequence, the decay routes are modified: for Hg and Tl, the state $[4f_{7/2}^{-1}5p_{1/2}]_3$ (purple) decays to $[4f^{14}5s5p_{1/2}]_1$ (gray) via M2 and to $[4f^{14}5s5p_{3/2}]_0$ (red) via E3. So that, the A-values are very small, resulting the much longer lived meta-stable states. Such losses of decay channels arising from level crossings also represent a more general phenomenon observed in other isoelectronic sequences, such as sliver (Ag), indium (In)-like [30] and palladium (Pd)-like [29] sequences.

However, for state $[4f_{7/2}^{-1}5p_{1/2}]_4$ (yellow), two decay

channels are identified: one proceeds via an E3 transition to state $[4f^{14}5s5p_{1/2}]_1$ (gray), and the other via an M1 transition to state $[4f_{7/2}^{-1}5p_{1/2}]_3$ (purple). Despite the occurrence of an energy crossing, as seen in Fig. 4, for Sm-like Hg and Tl ions, the energy level of $[4f_{7/2}^{-1}5p_{1/2}]_4$ (yellow) remains higher than that of $[4f^{14}5s5p_{1/2}]_1$ (gray) and $[4f_{7/2}^{-1}5p_{1/2}]_3$ (purple). Therefore, the primary decay channels of $[4f_{7/2}^{-1}5p_{1/2}]_4$ (yellow) are independent of $[4f^{14}5s5p_{3/2}]_2$ (green) and remain unchanged. Consequently, for Sm-like Hg-Po ions, the relatively small A-values associated with the M1 and E3 transitions account for the consistently low Out-rad rates.

5. Summary

In summary, we investigated and compared the soft X-ray spectra of Sm-like Bi^{21+} and Pb^{20+} in the water-window region using CoBIT-II. To assign the observed spectral lines, spectral simulations were performed based on CRM and atomic process is calculated by HULLAC. The calculations revealed that within the water-window range, both Sm-like Bi^{21+} and Pb^{20+} exhibit the same $4f-7g, 6g, 5g$, and $4d-5p$ transitions. In addition, CRM results showed that Pb^{20+} possesses three meta-stable states, $[4f^{14}5s5p_{1/2}]_0$, $[4f_{7/2}^{-1}5p_{1/2}]_4$ and $[4f_{7/2}^{-1}5p_{1/2}]_3$, the last is not meta-stable state in Bi^{21+}.

To explore the origin of this additional meta-stable state, further CRM calculations were carried out for Sm-like ions from Hg^{18+} to Po^{22+} using the same set of configurations. The soft X-ray spectra of Sm-like Hg-Po in the water-window region were simulated, predicting strong ground-state emissions from the $4f-7g, 6g, 5g, 4d-5p$ and $4d-4f$ transitions. In addition, for Tl^{19+} and Hg^{18+}, relatively strong $4f-5g$ emission lines originating from meta-stable states $[4f_{5/2}^{-1}5p_{1/2}]_4$ and $[4f_{5/2}^{-1}5p_{1/2}]_3$ were also predicted. For the meta-stable states $[4f_{5/2}^{-1}5p_{1/2}]_3$ and $[4f_{5/2}^{-1}5p_{1/2}]_4$ of Sm-like ions, the population decrease with atomic number. As the atomic number increases, the in-flow rate decrease, while the out-flow rate due to collisional (de)excitation also decrease but are offset by an increasing radiative decay rate. Consequently, the overall population diminishes with increasing atomic number. However, for meta-stable state $[4f^{14}5s5p_{1/2}]_0$, with increasing atomic number the out-flow rate due to collisional (de)excitation decrease, so that the overall population decrease.

[1] S.A. Golyshev *et al.*, Acta Naturae **15**, 32 (2023).
[2] J. Neethirajan *et al.*, Phys. Rev. X **14**, 031028 (2024).
[3] A. Botrugno *et al.*, Nucl. Instrum. Methods Phys. Res. A **623**, 747 (2010).
[4] H. Hara *et al.*, APL Photonics **2**, 086106 (2017).
[5] H. Kawasaki *et al.*, AIP Adv. **10**, 065021 (2020).
[6] T. Higashiguchi *et al.*, Appl. Phys. Lett. **100**, 014103 (2012).
[7] M.S. Safronova *et al.*, Phys. Rev. Lett. **113**, 030801 (2014).
[8] A. Botrugno *et al.*, Nucl. Instrum. Methods Phys. Res. A **623**, 747 (2010).
[9] D. Kato *et al.*, Nucl. Instrum. Methods Phys. Res. B **408**, 16 (2017).
[10] F. Zhou *et al.*, J. Phys. B **50**, 215001 (2017).
[11] W. Li *et al.*, Phys. Rev. A **91**, 062501 (2015).
[12] M. Mita *et al.*, J. Phys. Conf. Ser. **875**, 012019 (2017).
[13] D. Song *et al.*, J. Quant. Spectrosc. Radiat. Transfer **347**, 109621 (2025).
[14] N. Nakamura *et al.*, Rev. Sci. Instrum. **79**, 063104 (2008).
[15] H.A. Sakaue *et al.*, J. Instrum. **5**, C08010 (2010).
[16] A. Bar-Shalom *et al.*, J. Quant. Spectrosc. Radiat. Transfer **71**, 169 (2001).
[17] C. Yamada *et al.*, Rev. Sci. Instrum. **77**, 066102 (2006).
[18] Shimadzu Corporation. Laminar-type replica diffraction gratings for soft x-ray region (table of code numbers). https://www.shimadzu.com/opt/products/dif/od0gjn00000046ip.html (2025).
[19] A. Kramida *et al.*, NIST Atomic Spectra Database (ver. 5.12). https://physics.nist.gov/asd (2024).
[20] I. Hughes *et al.*, *Measurements and Their Uncertainties: A Practical Guide to Modern Error Analysis* (Oxford University Press, Oxford, UK, 2010).
[21] Baseline with asymmetric least squares (pro)—originlab documentation. https://www.originlab.com/doc/App/Baseline-with-ALS (2025).
[22] R. Garnett, *Bayesian Optimization* (Cambridge University Press, 2023).
[23] Q. Lu *et al.*, Phys. Rev. A **99**, 042510 (2019).
[24] C.-L. Yan *et al.*, Phys. Rev. A **105**, 032820 (2022).
[25] C. Wu *et al.*, Phys. Rev. A **111**, 042818 (2025).
[26] N. Kimura *et al.*, Phys. Rev. A **108**, 032818 (2023).
[27] A. Windberger *et al.*, Phys. Rev. A **94**, 012506 (2016).
[28] F. Torretti *et al.*, Phys. Rev. A **95**, 042503 (2017).
[29] N. Kimura *et al.*, Phys. Rev. A **102**, 032807 (2020).
[30] M.S. Safronova *et al.*, Phys. Rev. A **90**, 042513 (2014).